lineated than those of Chl*a*, consistent with the assertion that C_{phy} represents true variability in phytoplankton biomass.

Chl*a* monthly anomalies within the PSO (Fig. 3.23b) show variations of ±10% (± 0.015 mg m^{-3}) over the multi-mission time series, with largest deviations generally associated with El Niño/La Niña events. This link between ENSO variability and mean Chl*a* response in the PSO is demonstrated by the correspondence of anomaly trends with the Multivariate ENSO Index [(MEI; Wolter and Timlin (1998); presented in the inverse to illustrate the correlation, with R = −0.44)]. For 2018, Chl*a* anomalies were relatively small (±3%), consistent with weak ENSO conditions. Similar comments can be made about the C_{phy} anomaly trends, which show nominal to slightly elevated values in 2018 and also track well with the MEI over the 21-year timeseries (R = −0.39).

Variability and trends in Chl*a* reflect both adjustments in phytoplankton biomass and physiology (or health), while C_{phy} reflects changes in biomass alone. Both of these properties are mechanistically linked to physical conditions of the upper ocean, as well as to ecological interactions between phytoplankton and their zooplankton predators. Unraveling the diversity and covariation of factors that influence Chl*a* concentrations is essential for correctly interpreting the implications of Chl*a* anomalies on ocean biogeochemistry and food webs. For example, inverse relationships between Chl*a* and SST can emerge from changes in either mixed-layer light levels or vertical nutrient flux, but these two mechanisms have opposite implications on phytoplankton NPP (Behrenfeld et al. 2015). An additional complication is that measured changes in ocean color often contain a contribution from colored dissolved organic matter (Siegel et al. 2005) or from the changing phytoplankton population, with its type-specific optical characteristics (Dierssen 2010) that can be mistakenly attributed to changes in Chl*a* (Siegel et al. 2013). C_{phy} provides a more direct measurement of phytoplankton biomass that is insensitive to changes in physiological status of the cell, and thus offers complementary information on the state of the oceans. Future satellite missions, such as the planned hyperspectral Plankton, Aerosol, Cloud, ocean Ecosystem mission (PACE), will enable the rigorous separation of phytoplankton absorption features from non-algal features, as well as the assessment of changes in phytoplankton species or functional group distributions (Werdell et al. 2019). Such data will provide a major step forward in our ability to disentangle the impacts of climate forcing on global phytoplankton communities.

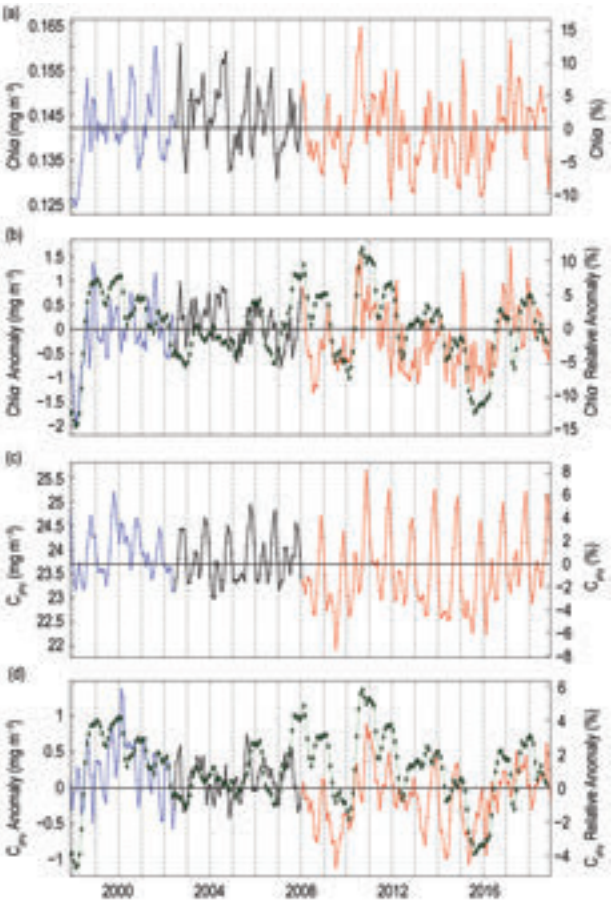

Fig. 3.23. 21-year, multi-mission record of Chl*a* and C_{phy} averaged over the PSO for SeaWiFS (blue), MODISA (red), and combined (black). Panel (a) shows Chl*a* from each mission, with horizontal line indicating the multi-mission mean Chl*a* concentration for the region. Panel (b) shows the monthly Chl*a* anomaly from SeaWiFS and MODISA after subtraction of the 20-year multi-mission climatological mean (Fig. 3.22). Panel (c) and (d) show the same as (a) and (b) respectively, but for C_{phy}. Green diamonds show the MEI, inverted and scaled to match the range of the Chl*a* and C_{phy} anomalies.

i. Global ocean carbon cycle—R. A. Feely, R. Wanninkhof, B. R. Carter, P. Landschützer, A. J. Sutton, C. Cosca, and J. A. Triñanes

The global oceans play a major role in the global carbon cycle by taking up a significant fraction of the excess CO_2 humans release into the atmosphere every year. As a consequence of humankind's collective release of CO_2 emissions into the atmosphere from fossil fuel burning, cement production, and land use changes over the last two-and-a-half centuries, commonly referred to as "Anthropogenic CO_2 (C_{anth})," the atmospheric CO_2 concentration has risen from pre-industrial levels of about 278 ppm (parts per million) to about 408 ppm in 2018. The

atmospheric concentration of CO_2 is now higher than has been observed on Earth for at least the last 800 000 years (IPCC 2013). As discussed in previous *State of the Climate* reports, the global ocean is a major long-term sink for C_{anth}, which is the major cause of ocean acidification. Here the discussion is updated to include recent estimates of that sink. Over the last decade, the global ocean has continued to take up a substantial fraction of the C_{anth} emissions and therefore is a major mediator of global climate change. Of the 10.8 (±0.9) Pg C yr^{-1} C_{anth} released during the period 2008–17, about 2.4 (±0.5) Pg C yr^{-1} (22%) accumulated in the ocean, 3.2 (±0.8) Pg C yr^{-1} (29%) accumulated on land, and 4.7 (±0.1) Pg C yr^{-1} (44%) remained in the atmosphere with an imbalance of 0.5 Pg C yr^{-1} (Le Quéré et al. 2018). This decadal ocean carbon uptake estimate is a consensus view based on a combination of measured decadal inventory changes, models, and global air–sea CO_2 flux estimates based on surface ocean partial pressure of CO_2 (pCO_2) measurements from ships and moorings. Using ocean general circulation models that include biogeochemical parameterizations (OBGCMs) and inverse models that are validated with observations-based air–sea exchange fluxes and basin-scale ocean inventories, Le Quéré et al. (2018) have demonstrated that the oceanic C_{anth} sink has grown from 1.0 (±0.5) Pg C yr^{-1} in the 1960s to 2.5 (±0.5) Pg C yr^{-1} in 2017. Air–sea CO_2 flux studies reported here and shown in Fig. 3.24 indicate a greater ocean uptake than provided in Le Quéré et al. (2018), due to an increased estimate of 0.78 Pg C yr^{-1} riverine contribution. This higher estimate in carbon from rivers is applied to the whole time series shown in Fig. 3.24.

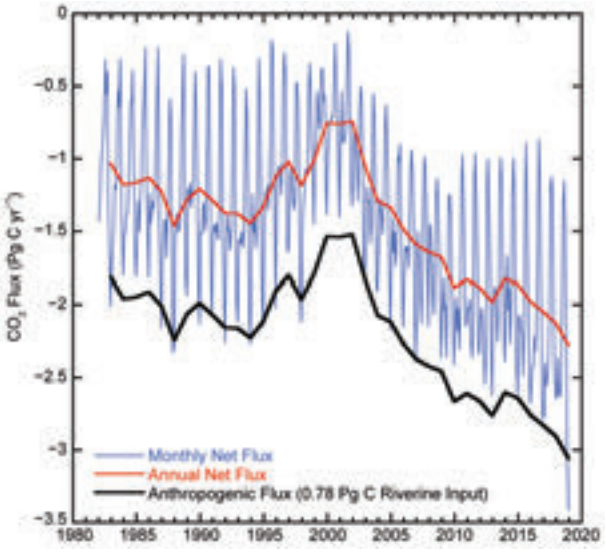

Fig. 3.24. Global annual (red line) and monthly (blue line) net CO_2 fluxes (Pg C yr^{-1}) for 1982–2018. The black line is the anthropogenic CO_2 flux, which is the net flux minus the riverine component of 0.78 Pg C yr^{-1}. Negative values indicate CO_2 uptake by the ocean.

1) Air–sea carbon dioxide fluxes

Ocean uptake of C_{anth} can be estimated from the net air–sea CO_2 flux derived from the bulk flux formula with air–sea differences in CO_2 partial pressure (ΔpCO_2) and gas transfer coefficients as input. A steady contribution of carbon from riverine runoff, originating from organic and inorganic detritus from land, revised upward from 0.45 to 0.78 Pg C yr^{-1} (Resplandy et al. 2018) is included to obtain the C_{anth} uptake by the ocean. The data sources for pCO_2 are annual updates of surface water pCO_2 observations from the Surface Ocean CO_2 Atlas (SOCAT) composed of mooring and ship-based observations (Bakker et al. 2016) and the Lamont-Doherty Earth Observatory (LDEO) database with ship-based observations (Takahashi et al. 2017). The increased observations and improved mapping techniques, including neural network methods and self-organizing maps (Landschützer et al. 2013, 2014; Rödenbeck et al. 2015), provide global pCO_2 fields on a 1° x 1° grid at monthly time scales annually. This allows investigation of variability on sub-annual to decadal time scales. The ΔpCO_2 and a parameterization of the gas transfer with wind described in Wanninkhof (2014) are used to calculate the air–sea CO_2 fluxes.

The monthly 2018 ΔpCO_2 maps are based on an observation-based neural network approach of Landschützer et al. (2013, 2014). The 2018 values are projections based on surface temperature, sea surface salinity, climatological mixed-layer depth, satellite chlorophyll-*a*, atmospheric CO_2, and the neural network for seawater pCO_2 developed from the data from the previous three decades. Changes in winds over time have a small effect on annual global air–sea CO_2 fluxes (Wanninkhof and Triñanes 2017). The C_{anth} fluxes from 1982 to 2018 suggest a decreasing ocean sink in the first part of the record and a strong increase from 2001 onward that continued into 2018 (Fig. 3.24). The amplitude of seasonal variability is large (≈ 1 Pg C) compared to the long-term trend with minimum uptake in the June–September timeframe. The C_{anth} air–sea flux of 3.1 Pg C yr^{-1} in 2018 is 36% above the revised 1996–2016 average of 2.24 (±0.4) Pg C yr^{-1}.

The average fluxes in 2018 (Fig. 3.25a) show the characteristic pattern of effluxes in the tropical regions and in the high-latitude Southern Ocean around 60°S, and uptake at mid-latitudes. The region with largest efflux is the equatorial Pacific. Coastal upwelling regions including the Arabian Sea, off the

coast of Mauritania, and the Peruvian upwelling system are significant CO_2 sources to the atmosphere as well. Large sinks are observed poleward of the subtropical fronts, and the frontal position determines the location of a maximum that is farther south and weaker in the Pacific sector of the Southern Ocean compared to the other basins.

In the Northern Hemisphere, there is a significant asymmetry in the sub-Arctic gyre with the North Atlantic being a large sink while the North Pacific is a significant source of CO_2. This is due in part to the position of the western boundary currents that are known CO_2 sinks at high latitudes. The Gulf Stream/North Atlantic drift extends farther north than the Kuroshio.

Ocean carbon uptake anomalies (Fig. 3.25b) in 2018 relative to the 1996–2016 average are attributed to the increasing ocean CO_2 uptake with time (Fig. 3.24) and to variations in large-scale climate modes. The long-term air–sea flux trend since 2000 is −0.7 Pg C decade^{-1} (or −0.16 mol m^2 yr^{-1} decade^{-1}), which leads to predominantly negative flux anomalies (greater ocean uptake). Despite this trend there are several large regions showing positive anomalies for 2018, notably the eastern equatorial Pacific, the subtropical North and South Pacific, and the high-latitude Southern Ocean. The increased effluxes in the eastern equatorial Pacific are related to a predominant negative sign of the Oceanic Niño Index (ONI) that followed an extensive period of predominantly positive ONI (El Niño) conditions in the preceding 20 years. This is borne out by the colder SST values (Fig. 3.26a) that indicate increased upwelling of waters with high CO_2 content. Positive anomalies in the Pacific subtropical regions (Fig. 3.25b) are related to the warm SST anomalies over the past year compared to the long-term average (Fig. 3.1a).

The differences between the air–sea CO_2 fluxes in 2018 compared to 2017 (Fig. 3.25c) are appreciable with anomalies roughly in the same regions as the difference of 2018 compared to the 20-year average. This indicates that conditions in 2018 are unique as compared to annual and decadal means. The increase in CO_2 effluxes in the eastern equatorial Pacific from 2017 to 2018 are associated with a return to more upwelling favorable conditions after the stalled El Niño in 2017. The Southern Ocean (south of 40°S) shows an increasing sink in the polar front region (≈ 50°S) and increasing source to the south for all three basins. The increasing sink near the polar front is partially compensated by a decreasing sink to the north. The correlations with SST anomaly (SSTA) are more nuanced. The large negative SSTA in the eastern South Pacific centered at 60°S is attributed to deeper convection and upwelling contributing to the positive CO_2 flux anomaly (Fig. 3.25b). However, the large positive CO_2 flux anomaly in the eastern South Atlantic sector does not have a strong SSTA associated with it. The band of negative flux CO_2 anomalies compared to 2017 centered near 50°S is in a region with predominantly positive SSTA that suggests that in this band, SSTA and flux anomalies are decoupled. The North Pacific shows a large decrease in sink strength roughly following the path of the Kuroshio Current with a positive SSTA.

As detailed above, many of the pCO_2 and flux anomalies can be attributed to variations in large-scale climate modes and associated physical anomalies, notably temperature, but the causality is often

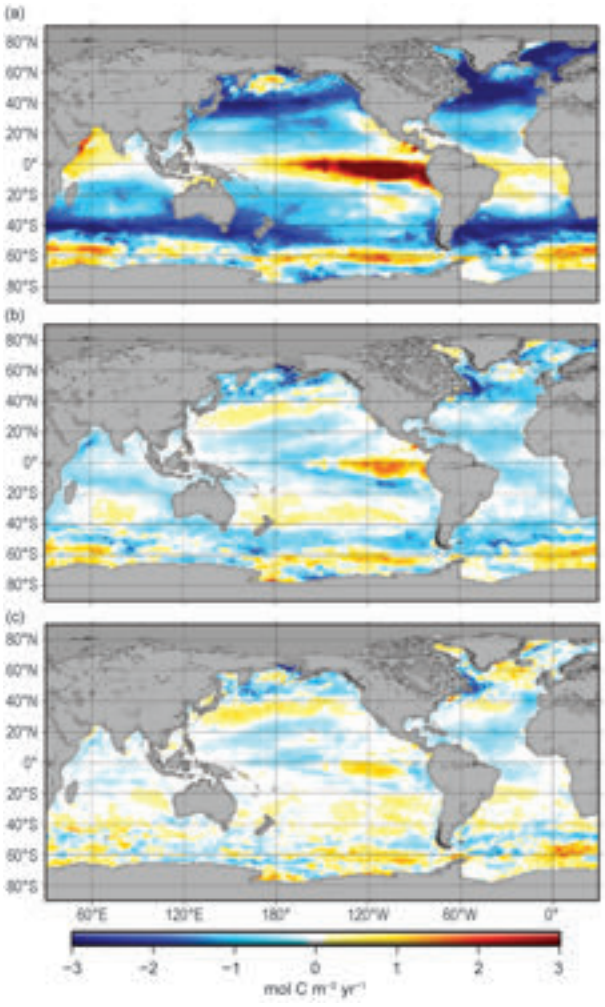

Fig. 3.25. Global map of (a) net air–sea CO_2 fluxes for 2018, (b) net air–sea CO_2 flux anomalies for 2018 relative to a 1996–2016 average, and (c) net air–sea CO_2 flux anomalies for 2018 minus 2017 values following the method of Landschützer et al. (2013), all in mol C m^{-2} yr^{-1}.

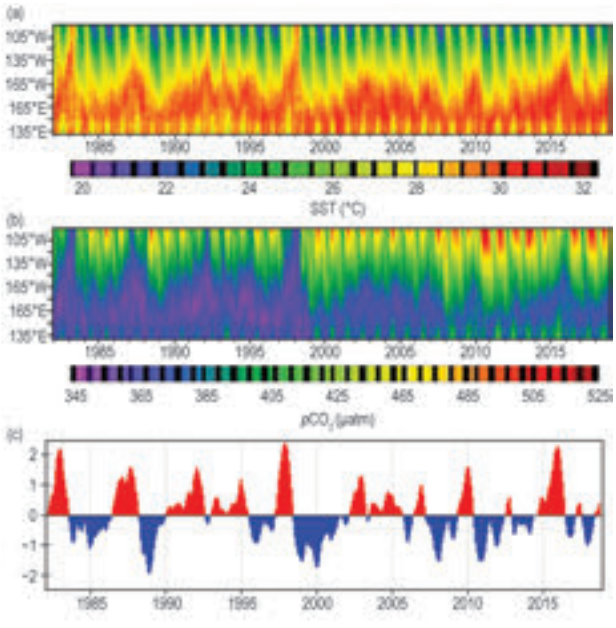

Fig. 3.26. Time-longitude plots of: (a) SST, (b) pCO_2, and the (c) ONI from 1982–2018 in the equatorial Pacific. Significant reductions in surface water pCO_2 values (low CO_2 outgassing) correspond with the El Niño events of 1982–83, 1986–87, 1991–94, 1997–98, 2002–05, 2006–07, 2009–10, and 2015–16. Significant enhancement of the pCO_2 values (high CO_2 outgassing) occurred with the strong La Niña events in 1984–85, 1998–99, 1995–96, 1998–2000, 2007–08, and 2011–12. 2018 was a normal non-El Niño year.

complex. For example, the behavior of pCO_2 with respect to temperature includes competing processes: thermodynamics dictate decreasing pCO_2 with decreasing SST, but waters originating from the deep with a cold temperature signal will have a high pCO_2. Moreover, the drawdown of pCO_2 due to biology is often associated with increasing temperature, but this depends on region and season.

The strong trend of increasing CO_2 uptake since 2002 has continued through 2018 with an increase of 0.15 Pg C above the 2017 estimate. This increase is well within the uncertainty of the estimate, but it is within the overall expectation that the ocean will remain an increasing sink as long as atmospheric CO_2 levels continue to rise. The sequestration of CO_2 by the ocean partially mitigates the atmospheric CO_2 rise, but it comes at a cost of increased acidification of surface and subsurface waters (Carter et al. 2017).

2) Interannual variability of pCO_2 in the tropical Pacific

From previous studies in the tropical Pacific, it is well-established that the oceanic variability of the air–sea exchange fluxes in this region are largely controlled by the surface ocean pCO_2 variability and wind forcing influenced by the nature and phasing of ENSO events (e.g., Feely et al. 1999, 2002, 2006; Ishii et al. 2009, 2014; Takahashi et al. 2009; Wanninkhof et al. 2013; Landschützer et al. 2014, 2016). The central and eastern equatorial Pacific is a major source of CO_2 to the atmosphere during non-El Niño and La Niña periods; it is near neutral during strong El Niño periods, and a weak source during weak El Niño periods. The warm El Niño phase of the ENSO cycle is characterized by a large-scale weakening of the trade winds, decrease in upwelling of CO_2 and nutrient-rich subsurface waters, and a corresponding warming of SST in the eastern and central equatorial Pacific. The opposite phase of the ENSO cycle, called La Niña, is characterized by strong trade winds, cold tropical SSTs, and enhanced upwelling along the equator. Figure 3.26 shows time-longitude plots of SST and pCO_2 for the region from 5°N to 10°S and 130°E to 95°W, and the Oceanic Niño Index (ONI) for the 36-yr period from 1982 through 2018. During the strong eastern Pacific El Niño events of 1982–83, 1997–98, and 2015–16, the cold waters of the eastern equatorial Pacific disappear and pCO_2 values are close to equilibrium with the atmosphere. However, during the weaker central Pacific El Niños of 1991–94, 2002–05, and 2006–07, the equatorial cold tongue is present but less pronounced, and pCO_2 values are higher than atmospheric values but lower than corresponding values for non-El Niño periods. The strongest El Niño event of 1997–98 had SST anomalies exceeding 4°C and the lowest pCO_2 values throughout most of the equatorial Pacific. In contrast, the 2015–16 El Niño event had SST anomalies that are similar to the 1997–98 event, yet the pCO_2 values were significantly higher because the upwelling-favorable winds were stronger in the easternmost and westernmost parts of the region. By 2018, the region returned to non-El Niño conditions and near-normal pCO_2 levels.

3) Long-term trends of surface ocean pCO_2

Another feature of the time series of pCO_2 measurements in the Pacific is the secular increase of oceanic pCO_2 in response to the rise in atmospheric CO_2. Studies from surface ships and moorings have demonstrated de-seasoned secular increases of surface ocean pCO_2 ranging from 2.3–3.3 μatm yr^{-1}; however, rates of change are lower during El Niño periods and higher during La Niña periods (Feely et al. 2006; Sutton et al. 2014). The highest rates of increase are observed in the eastern Pacific near 125°W. In the tropical Pacific, the strong influence of interannual and decadal variability on surface ocean pCO_2 makes it challenging to detect the anthropogenic change.

In the subtropical Pacific, time-series observations are long enough to detect the anthropogenic signal above the natural variability of the ocean carbon system (Sutton et al. 2017, 2019). De-seasoned monthly means of surface ocean pCO_2 observations at the Woods Hole Oceanographic Institution Hawaii Ocean Time-series Station (WHOTS) in the subtropical North Pacific and Stratus in the South Pacific gyre show anthropogenic trends of 1.8 ± 0.3 µatm yr^{-1} and 2.0 ± 0.3 µatm yr^{-1}, respectively (Fig. 3.27). These trends are not significantly different from each other or from the atmospheric (xCO_2) rate of increase at Mauna Loa Observatory of 2.2 ppm over this same time period.

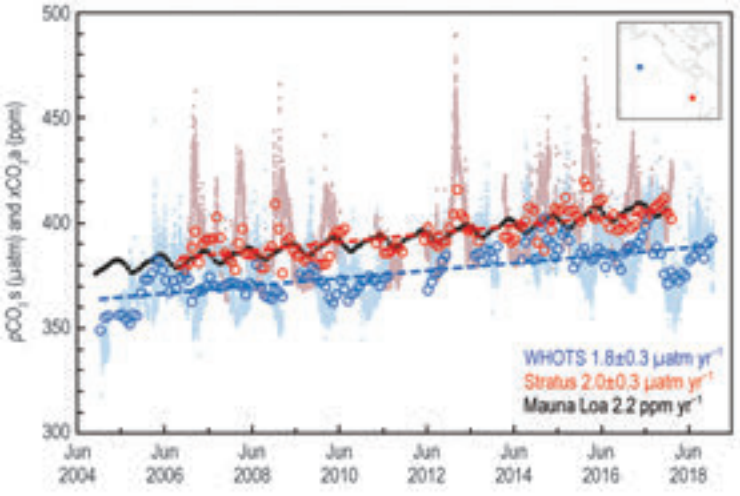

Fig. 3.27. Moored time-series observations of surface ocean seawater pCO_2 (pCO_2s) at the WHOTS (blue) and Stratus (red) sites in the subtropical Pacific (inset). Light colors are the high-resolution measurements and circles represent de-seasoned monthly means. Dashed lines represent trend of de-seasoned values. As a reference, the climate record of atmospheric CO_2 (xCO_2a) from Mauna Loa Observatory is shown in black (NOAA ESRL Global Monitoring Division, 2017).

4) Global ocean carbon inventories

Synoptic ship-based hydrographic measurements are the primary data with which the ocean carbon inventory, its anthropogenic component, and their changes are calculated. Ocean carbon inventories were first quantified in detail as part of the mid-1990s World Ocean Circulation Experiment (WOCE). The Climate Variability (CLIVAR) Repeat Hydrography Program in the mid-2000s and the Global Ocean Ship-based Hydrographic Investigations Program (GO-SHIP) since 2010 have re-measured a subset of the ocean-basin-spanning hydrographic cruise-tracks needed to update the inventories. Critically, these three programs each provided synoptic measurements of a range of seawater parameters with sufficient accuracy and spatial density (vertically and horizontally) in consistent locations to constrain anthropogenic carbon inventory changes with high confidence.

During the last year, a major analysis was completed quantifying the oceanic sink for CO_2 between 1994 and 2007 (Gruber et al. 2019). It was enabled by recent refinements to methods for processing interior ocean carbon data (e.g., Clement and Gruber 2018) and a data product released as the culmination of a decade of ship-based data synthesis and quality control work (Olsen et al. 2016). The analysis finds that ocean inventory increased by 34 (±4) PgC (i.e., 10^{15} g carbon) over this span at an average rate of 2.6 (±0.3) PgC year^{-1}. The scientists project this rate forward to estimate a global inventory for the year 2010 of 160 (±20) PgC. These findings are consistent with recent findings based on combinations of models and data (Khatiwala et al. 2013) and inversions of a variety of data types (DeVries et al. 2017). The rate of storage is increased relative to periods prior to 1994, but consistent with expectations from steadily increasing atmospheric CO_2 concentrations. However, broad regional variations were observed in the rate of CO_2 accumulation, suggesting that variability in ocean circulation and other modes of climate variability have important effects on ocean carbon concentrations on decadal timescales.

The patterns of accumulation vary by ocean basin (Fig. 3.28) in a manner consistent with broad-scale ocean circulation features, with significantly higher accumulation in shallower waters and in the warmer subtropical gyres, and less accumulation in the regions where dense waters upwell near the equator and in the subpolar oceans and the Southern Ocean. Higher accumulation occurs in shallower waters due to the close contact with the atmosphere, and slower accumulation occurs in upwelling waters that have been out of contact with the changing atmosphere for longer. As a secondary impact, higher accumulation occurs in warmer waters because elevating seawater chemistry drives reactions and gas exchange that result in the waters being more well-buffered against changing pCO_2, meaning atmospheric pCO_2 increases elevate the total carbon content of seawater by a larger amount before the seawater approaches air–sea equilibrium.

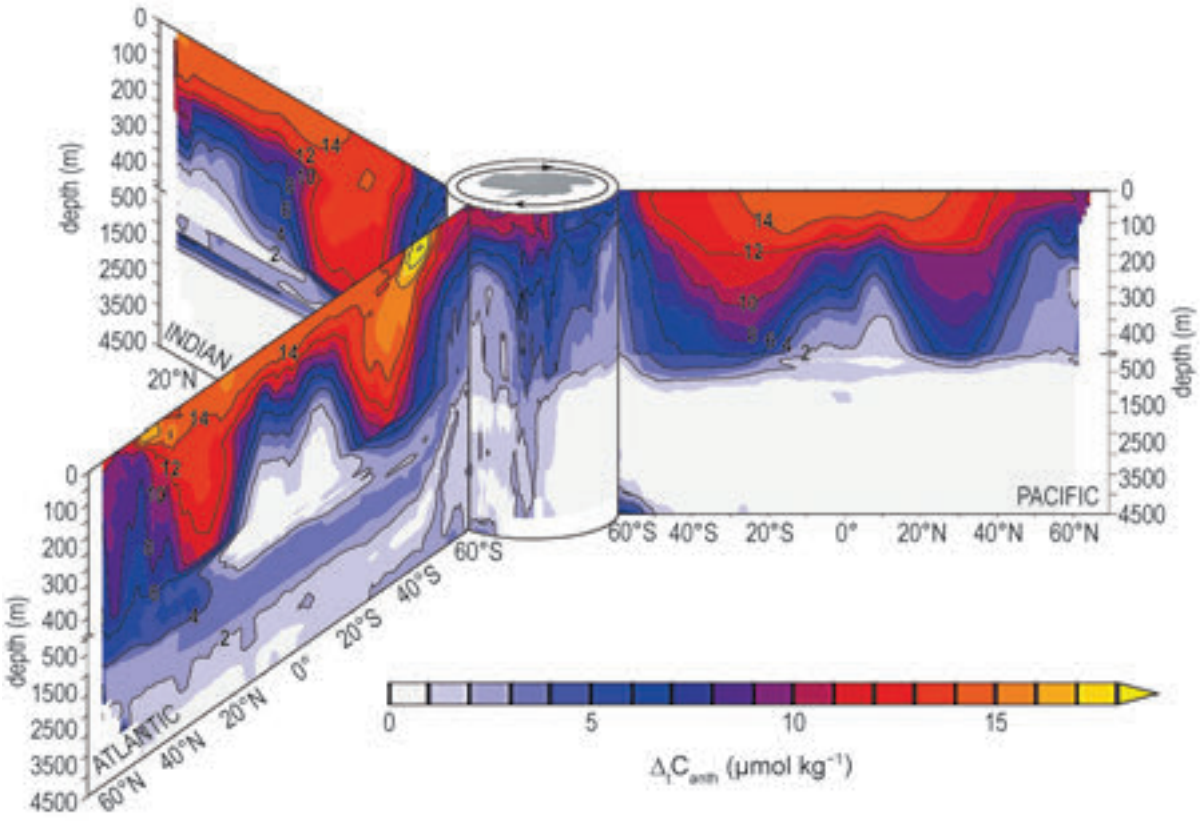

Fig. 3.28. Vertical sections of the accumulation of anthropogenic carbon in µmol kg^{-1} between the WOCE and CLIVAR periods of the repeat hydrographic records, as inferred by Gruber et al. (2019). Shown are the zonal mean sections in each ocean basin organized around the Southern Ocean (center). The upper 500 m are expanded and contour intervals are spaced at 2 µmol kg^{-1} of C_{anth}.